Mechanics of Materials 181 (2023) 104640

Contents lists available at ScienceDirect

Mechanics of Materials

journal homepage: www.elsevier.com/locate/mechmat

Thermomechanical characteristics of green nanofibers made from polylactic acid: An insight into tensile behavior via molecular dynamics simulation

Razie Izadi [a], Meral Tuna [a], Patrizia Trovalusci [a,*], Nicholas Fantuzzi [b]

[a] Department of Structural and Geotechnical Engineering, Sapienza University of Rome, Via A. Gramsci, 53, 00197, Rome, Italy
[b] Department of Civil, Chemical, Environmental and Materials Engineering, University of Bologna, Viale del Risorgimento 2, Bologna, 40136, Italy

ARTICLE INFO

Keywords:
Molecular dynamics simulation
Tensile deformation
Fracture mechanics
Thermomechanical property
Polymer nanofiber

ABSTRACT

All-atom molecular dynamics simulations are conducted to elucidate the thermomechanical characteristics of polylactic acid nanofibers with a diameter range of 1.93 nm–5.4 nm. Nanofibers undergo tensile deformations from which elastic, yield, softening and fracture phases are recognized and mechanical parameters are evaluated by tracking the stress, energy and geometrical evolutions at each phase. Special attention is devoted to the fracture phase where a new method is proposed to calculate the energy release rate during crack propagation which is a crucial factor in fracture mechanics. The effect of nanofibers' diameter, temperature and the deformation strain rate on fracture properties, moduli of resilience and toughness, yield stress, Young's modulus and Poisson's ratio is studied. Monitoring the variation of the internal energy components during deformation reveals the dominance of bond and van der Waals contributions in the deformation mechanism. Finally, a comparison of nanofiber parameters with that of the bulk polymer shows that compared to the thermal properties, the mechanical parameters are more affected by the confinement of the nanofibers.

1. Introduction

Polymer nanofibers (PNFs), with diameters less than 100 nm (nm), are widely used in diverse areas of science due to their unique characteristics and improved properties compared to the macroscopic counterparts (Chew et al., 2006; Carlisle et al., 2009, 2010; Baker et al., 2016; Wong et al., 2008, 2009; Guhados et al., 2005) (Li and Wan, 2017). Currently, nanofibers, whether freestanding or as non-woven mats, are of great interest in tissue engineering (Agarwal et al., 2009; Lannutti et al., 2007; Stevens and George, 2005; Place et al., 2009), composite reinforcements (Ajayan et al., 2006), sensors (Ding et al., 2009; Sagadevan and Periasamy, 2014), filtration (Gopal et al., 2006; Yun et al., 2007), drug delivery (Place et al., 2009), wound dressing, and so many other practices (Huang et al., 2003).

Among PNFs, special attention is devoted to those constructed from poly (lactic acid) (PLA) due to the biodegradability and non-toxicity of lactic acid, which already exists in the human body, and is approved by FDA for the manufacturing of bioresorbable surgical sutures and biomedicine (Abdal-hay et al., 2013; Sarapirom et al., 2014; Abdal-Hay et al., 2016; Blasi, 2019; Tyler et al., 2016). PLA is an ideal candidate for loading drug molecules (Han et al., 2018) or mimicking extracellular matrix for tissue engineering scaffold (Abdal-Hay et al., 2016; Santoro et al., 2016). It is also used to produce nanocomposites with noticeable shape memory effects (Sonseca et al., 2017).

Different processing methods are currently established for the production of PNFs, including mechanical drawing, template synthesis, phase separation, self-assembly, and electrospinning (Jayaraman et al., 2004), among which the latter provides an efficient method to massively produce bioengineered nanofibers with diameters down to only several nanometers (Wang et al., 2013, 2017; Xue et al., 2017; Jahanmard-Hosseinabadi et al., 2018). Some experiments have even demonstrated the possibility of PNF production with a diameter of less than 1 nm through electrospinning. Huang et al. reported the production of nylon-4,6 nanofibers with diameters of 1.6 nm or less obtained from a semi-dilute concentration of 2%. (Huang et al., 2006). In an experiment by Jian et al. the cross-section analysis of electrospun nanofibers that are formed from dilute solutions (0.01 wt%) revealed the possibility of reducing diameters to even 0.17 nm (Jian et al., 2018).

* Corresponding author.
E-mail addresses: razie.izadi@uniroma1.it (R. Izadi), meral.tunaeroglu@uniroma1.it (M. Tuna), patrizia.trovalusci@uniroma1.it (P. Trovalusci), nicholas.fantuzzi@unibo.it (N. Fantuzzi).

https://doi.org/10.1016/j.mechmat.2023.104640
Received 23 December 2022; Received in revised form 25 March 2023; Accepted 28 March 2023
Available online 30 March 2023

It is crucial to characterize a single nanofiber independently as the properties of PNF-based materials stem from their intrinsic features and organization. Indeed, PNFs diameter, morphology, and thermo-mechanical character act on their functionality in diverse applications. For instance, it is reported that PNF's diameter affects its effectiveness in the drug delivery system (Chen et al., 2012). The stiffness of PNF artificial substrates influences cell growth, proliferation, and differentiation in tissue engineering. The strength and durability of PNF are critical factors in the fields of filtration, protective clothing, and fabrics (Rao et al., 2013; Engler et al., 2006; Mohammadzadehmoghadam et al., 2016).

So far, testing methods for PNFs mechanical characteristics include atomic force microscopy (AFM), three-point bending, nanoindentation, and nano-tensile and resonance contact-based test (Li and Wan, 2017). These conventional tests can be used for fibers with diameters larger than 20 nm (Li and Wan, 2017). However, as the nanofiber diameter decreases, their characterization through experiments faces so many challenges. For instance; in AFM cantilevers, it becomes challenging to anchor PNF on micro ridges to prevent slippage (Baker et al., 2016) and to apply the nano-force in proper position (Jahanmard-Hosseinabadi et al., 2018; Neugirg et al., 2016). Moreover, in nano-tensile test, it becomes challenging to mount single fibers to a conventional tensile tester and to have loadcells with sufficient sensitivity (range). (Li and Wan, 2017). Altogether, the requirements to characterize PNFs for the efficient design of PNF-based materials and the difficulty in experimental testing call for utilizing atomistic computer simulations, especially in small diameter PNFs. Molecular dynamics simulations (MD), as a popular branch of atomistic simulations, is widely used to study the molecular structure, function, and interaction of polymer material. (Huang et al., 2003). Through MD, a wide variety of thermodynamical, structural, and transport properties can be determined, providing valuable insight into nanoscopic structures' behavior.

Until now, only a limited number of studies have focused on implementing atomistic simulations to characterize the thermo-mechanical characterization of PNFs; Vao-soongnern et al. conducted the very first study to model polyethylene (PE) nanofibers through atomistic simulations. Using the coarse-grained Monte Carlo method on a high coordination lattice, they calculated surface energies as a function of the fiber radius (Vao-soongnern et al., 2000). However, the first attempt to model PNFs with MD can be attributed to the work by Curgul et al. (2007) in which the size-dependent glass transition temperature (Tg) of PE nanofibers with diameters less than 23.0 nm is studied through coarse-grained MD and united atom model. Consistent with experiments, Tg is reported to decrease with fiber diameter. Later, Buell et al. (2009) calculated Young's modulus and Poisson's ratio of glassy PE nanofibers with the diameters ranging from 3.7 nm to 17.7 nm at temperatures of 100 K and 150 K. Young's moduli of these nanofibers were found to decrease by decreasing fiber radius and the Poisson's ratio was reported to increase by increasing diameter in the range of 0.1–0.3. Milani et al. (2011) implemented a coarse-grained MARTINI force field (Marrink et al., 2007) to simulate nylon-6 nanofibers and to study their melting and re-crystallization. Tang et al. (2014) used MD simulation to determine Young's modulus and Poisson's ratio of a collection of bead−spring chains representing PNFs. Using the data extracted from MD, they adopted the finite element method and reported the formation of some rippling on the surface of nanofibers. Similar to the observation in (Buell et al., 2009), a decrease in Young's modulus with diameter is reported, whereas, in contrary to (Buell et al., 2009), they have showed that Poisson's ratio increases with decreasing diameter. Conversely, an increasing trend for elastic modulus with increasing diameter was found in an MD simulation by Deng et al. (2017). The effect of pre-stretching on the elastic modulus was also studied in their work. Later, Peng et al. (2019) presented the stress-strain curves and Young's moduli for PE nanofibers with diameters of 10 nm–19 nm. They tried to simulate hot-drawn PNFs using the same initial configuration and applying different strains in the fiber direction to achieve different diameters. Although an increase in Young modulus with the increase in diameter was observed for hot-drawn fibers, no size-dependency is encountered in the tensile test result of non-drawn three PE nanofibers with 10, 20, and 30 nm diameter. In a study conducted by Kwon and Sung (2020), a coarse-grained MD is adopted on a typical PNF with a 30 nm diameter, and the nonlinear mechanical response of the fiber and its dependence to strain rate is analyzed. Finally, in a recent publication by Liu et al. (2021), the tensile behavior of a special kind of nanofiber named as hierarchically twisted nanofiber is studied through coarse-grained MD and the effect of twisting angle is discussed.

Atomistic simulations can be conducted using coarse-grained or all-atom representations; in the former, a group of atoms is deemed as a single bead where the internal interaction inside the bead is passed over with its effect depicted in the bead's interactions. This will decrease the computational cost and allow for larger scales simulations in exchange for precision. However, in the latter, all the individual atoms are simulated which naturally increases the results reliability at the expense of the elevated computational cost. All the studies on molecular simulation of PNFs have adopted coarse-grained method and are limited to PE, with a single study on nylon-6 using coarse-grained simulations. However, the findings of different MD studies on the mechanical behavior of PNFs contradict each other, especially regarding the trend of Young's modulus versus diameter. Considering the above remarks, an all-atom precise simulation to study the mechanical and thermal response of PNFs is required. We have focused on PLA nanofiber as one the most popular nanofibers with a wide range of applications.

To the best of our knowledge, this is the first time that the thermo-mechanical characteristics of nanofibers made from biodegradable PLA is studied through all-atom molecular dynamics simulation. In the current contribution, a comprehensive simulation is conducted for small-diameter (1.9–5.4 nm) PLA nanofibers to study their tensile behaviour. During the tensile test, all the elastic, plastic and fracture phases are characterized and the corresponding material parameters in each phase are calculated including Young's modulus and Poisson's ratio, proportional and yield stresses, moduli of resilience and toughness. Focusing on the fracture phase, we have proposed a method to characterize the energy release rate in nanofibers which is a fundamental property in fracture mechanics analysis. The structural evolution during deformation is discussed alongside the effect of diameter, strain rate, and temperature. In addition to the mechanical parameters, the glass transition temperature and radial coefficient of thermal expansion are calculated with also providing a discussion on the internal energy components during the deformation mechanism. The rest of the paper is organized as follows; Section 2 describes the simulation methodology. The results on thermomechanical parameters accompanied by a comprehensive discussion are provided in Section 3. The remarks are summarized and concluded in Section 4.

2. Materials and methods

2.1. Polylactic acid

Molecular dynamics simulations are conducted using LAMMPS (Thompson et al., 2022) which enables spatial decomposition of domain on parallel processors, thus provides an efficient tool for simulating large-scale atomistic systems. Here, the initial structure of nanofibers and bulk state are constructed using Materials Studio software (BIOVIA, 2017). The present work focuses on nanofibers made of PLA, having the molecular formula $(C_3H_4O_2)_n$ (Lim et al., 2008) shown in Fig. 1, a biodegradable polymer obtained from renewable sources and agricultural products with very low toxicity (Martinez et al., 2011). PLA biocompatibility, along with desired thermomechanical performance and good processability, has allowed for its diverse and novel practices, especially in biomedical sectors (Maleki et al., 2022). In the current work, polymer nanofibers (PNFs) with diameters from 1.9 to 5.4 nm are constructed from different numbers of 20-monomer polymer chains

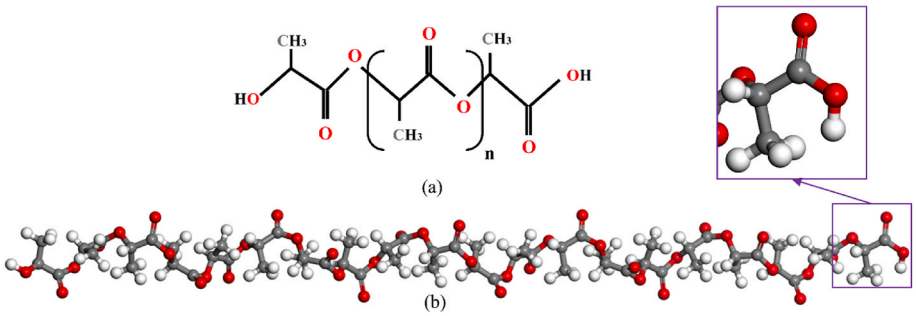

Fig. 1. a) Chemical structure of PLA b) PDLA stereoisomer of PLA.

(Fig. 1a). In the current work, we set the number n in Fig. 1a as 18 which gives a total 20 monomers.

Although common manufacturing processes produce PLA with much longer length and higher molecular weight (Mw), some biomedical applications require low Mw because high Mw PLA has a complete resorption time of two to eight years (Farah et al., 2016). This prolonged existence in vivo can lead to inflammation and infection in some organs (Bergsma et al., 1995). Therefore, the production of low Mw PLA is desirable because it has a shorter degradation rate. For instance, Andreopoulos et al. (2000) and Jabbari and He (2008), studied the effect of low molecular weight PLA (1200 g/mol and 2000–20,000 g/mol) to find the desired properties for drug delivery and degradable implants.

Due to the chirality of the lactic acid molecule, PLA has different stereoisomers, such as poly (L-lactide) (PLLA), poly (D-lactide) (PDLA), and poly (DL-lactide) (PDLLA) (Scaffaro et al., 2017; Tsuji, 2005; Auras et al., 2011). According to Fig. 1b, the polymer simulated in the current work is PDLA due to the relative position of the methyl group to the chain backbone (Klotz et al., 2016; Scaffaro et al., 2020). In contrast to PLLA, PDLA has no tendency for crystallization (Auras et al., 2011); Therefore, in the current work, nanofibers are in the amorphous state.

Although highly crystallized PLLA exhibits high strength, the amorphous nature of PDLA shows a faster rate of degradation, making it the preferred choice for applications as a drug delivery vehicle and as a low strength scaffold material for tissue engineering (Auras et al., 2011; Taib et al., 2022).

2.2. Interatomic potential

To describe atomic interactions, the *ab initio* class II polymer consistent forcefield (pcff) is assigned, which is proven to be useful for modelling polymers and organic materials (Sun, 1994; Sun et al., 1994). PCFF is known for characterizing well the cohesive energies, mechanical properties, compressibility, heat capacities, and elastic constants of polymers and organic substances (Peng and Zeng, 2017). As detailed in Eq. (1a-d), the total energy in PCFF (E_{PCFF}) splits into valence\bonded ($E_{valence}$), and non-bonded interactions ($E_{non-bonded}$);

$$E_{PCFF} = E_{valence} + E_{non-bonded} \tag{1a}$$

where the valence term includes bond (E_{bond}), angle (E_{angle}), dihedral ($E_{dihedral}$), inversion ($E_{inversion}$), and the cross-coupling ($E_{cross-coupling}$) interactions between atoms:

$$E_{valence} = E_{bond} + E_{angle} + E_{dihedral} + E_{inversion} + E_{cross-coupling} \tag{1b}$$

Bond and angle interactions contain up to quartic terms to characterize inharmonic features. A symmetric Fourier expansion is used for torsion interactions with a simple harmonic function to represent the out-of-plane contributions (Sun, 1995).

$$\begin{aligned} E_{bond} = \sum_{n=2}^{4} k_n^b (b - b_0)^n, E_{angle} = \sum_{n=2}^{4} k_n^\theta (\theta - \theta_0)^n, E_{dihedral} \\ = \sum_{n=2}^{4} k_n^\varphi (1 - \cos(n\varphi))^n, E_{inversion} = k^\chi (\chi - \chi_0)^2 \end{aligned} \tag{1c}$$

where k_i^j, represents i-th coefficient related to j-th kind of energy where the superscripts *b*, θ, φ and χ are assigned for bond, angle, dihedral and inversion. Details on cross-coupling term can be found in (Sun, 1995).

On the other hand, the non-bonded term encompasses electrostatic ($E_{electrostatic}$) interactions and a 9-6 Lennard-Jones potential representing the van der Waals forces ($E_{van\ der\ Waals}$).

$$\begin{aligned} E_{non-bonded} = E_{electrostatic} + E_{van\ der\ Waals}\ E_{van\ der\ Waals} \\ = \varepsilon \left[\left(\frac{\sigma}{r}\right)^9 - \left(\frac{\sigma}{r}\right)^6 \right] r < r_{cutoff} E_{electrostatic} = q_i q_j \Big/ r \end{aligned} \tag{1d}$$

where r is the distance in-between an atom pair, ε and σ are the well depth and zero-crossing distance for the potential and q_i is the charge of atom i. For all simulations, non-bonded interactions are truncated at a cutoff radius of $r_{cutoff} = 1$ nm (Prasitnok, 2016).

2.3. Initial configurations

2.3.1. PLA bulk state

Prior to creating nanofibers, a cuboid periodic simulation box with 10 polymer chains each containing 20 monomers representing the polymer bulk state is constructed using an Amorphous Cell Module in Materials Studio (BIOVIA, 2017) that builds molecules in a cell in a Monte Carlo manner by minimizing close contacts between atoms, while ensuring a realistic distribution of torsion angles for the given forcefield. This representative volume element (RVE) is initially constructed at a low density (0.3 g/cm^3) to avoid high energy interactions and then ramped up to a density of 1.3 g/cm^3, in accordance with literature (Farah et al., 2016) by following the subsequent procedure. First, energy minimization is directed through a smart algorithm which is a cascade of steepest descent, adjusted basis Newton-Raphson, and quasi-Newton method. Second, to enable higher mobility of polymer chains and speed up equilibration, the RVE temperature is increased and maintained at 500 K, which is estimated to be well above the glass transition temperature (Tg) of PLA (between 323 K and 353 K (Garlotta, 2001; Zohuri, 2012)). The temperature increase is performed through a canonical (NVT) ensemble where the total number of atoms, volume of the simulation box, and the temperature of the system are kept constant. An NPT ensemble which conduct isothermal-isobaric simulations at 1 atm and 500 K is then followed for 5 ns (ns). Finally, the system is cooled down to 298 K within 10 ns under constant pressure, where it reaches the final dimension of 16 × 16 × 76.2 Å^3 (Fig. 2a). The final average density is 1.237 g/cm^3, which agrees well with available data (between 1.21 and 1.3 (Farah et al., 2016)). For the bulk state, the Nose-Hoover thermostat and barostat are used to control the temperature and

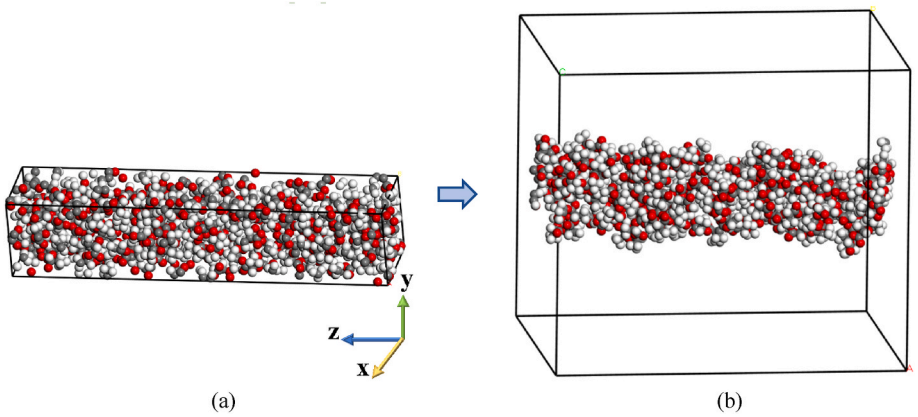

Fig. 2. a) Initial cuboid b) Relaxed nanofiber in the enlarged cell.

pressure with a time step of 1 fs (fs) using stochastic time integrator (Bussi et al., 2009). The thermostat and barostat damping parameters are set as 50 fs and 1000 fs as typical values used in molecular simulations (Yu et al., 2010).

2.3.2. PLA nanofibers

To construct PLA nanofibers, after equilibrium of the cuboid simulation box, using the "rebuild crystal" option in Materials Studio, the box dimension is increased 5–7 times the cutoff radius (1 nm) in the x and y direction without rescaling atom coordinates while the z direction dimension is remained unchanged. Consequently, the polymer atoms will not interact with their images in the x and y transverse directions (Fig. 2 -b). In this case, without altering the periodicity of the simulation box, through a further equilibration, we obtain a nanofiber isolated in lateral directions with infinite axial length due to periodicity in the z direction.

To build nanofibers with larger cross-sections, the initial equilibrated cuboid is replicated in the transverse directions 2 and 3 times, and then the procedure for enlargement of lateral dimensions is adopted again (Fig. 3a and b); in this way, the effect of diameter change can individually be evaluated without the interference of other factors like change of polymer chain alignments and entanglements.

The nanofiber structures were then inserted into a molecular dynamics code in LAMMPS with *msi2lmp* plugin (Thompson et al., 2022). An equilibration sequence is then performed on each polymer nanofibers prior to deformation, which involves four different steps (Izadi et al., 2019). First, the energy is minimized with the conjugate gradient method, then through NVT ensembles, the temperature is increased and maintained at 500 K and cooled back to 1 K within 1 ns, further, the temperature is increased and maintained at the desired value. The cooling rate is chosen following some current work on MD simulation of polymer (Hossain et al., 2010; Hasheminejad and Montazeri, 2020), however it should be noted that the cooling rate is high regarding the real production procedure and a parametric study on the effect of cooling rate is of help. The fiber lateral surface experiences unconstrained boundary conditions and is free to expand or contract regardless of the choice of the ensemble for the simulation box. For NVT dynamics of nanofibers, Langevin thermostat, with the damping parameter of 1 fs, is deployed as described in (Schneider and Stoll, 1978) which sets the temperature of the atoms while modeling an interaction with a background implicit solvent. A time step of 1 fs is used in the velocity-Verlet algorithm to integrate Newton's equations of motion.

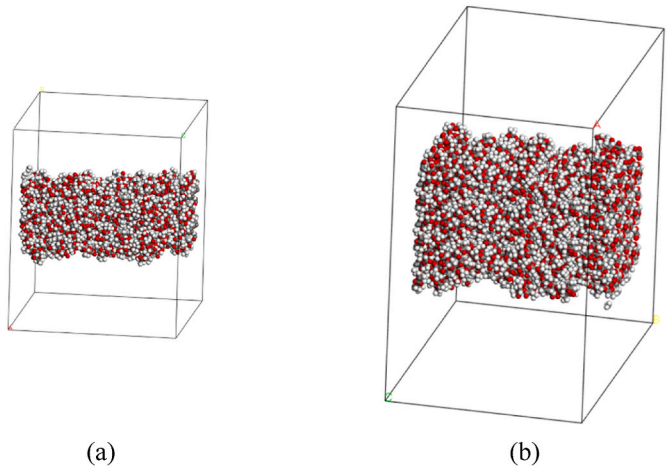

Fig. 3. PLA nanofibers with a) 3.2 × 3.2 nm^2 and b) 4.8 × 4.8 nm^2 initial cross sections.

2.4. Density radial distribution and effective radius (R_{eff})

To gain a better insight into the inner structure of nanofibers and determine their effective radii, the density profile along the radius is studied. In this respect, nanofibers cross-sections are divided into concentric cylindrical layers of 0.1 nm thickness (schematically in Fig. 4a). By counting the number of each atom kind fallen into the individual shell, the mass of each shell is calculated and normalized by its volume to obtain the mass density of every layer.

Analyzing the density radial distribution reveals the existence of a core region with a density near the bulk state (1.24 g/cm^3) embraced by a degrading low-density layer called the "surface layer" which is believed to be caused by the surface tension of nanofibers (Fig. 4b) (Curgul et al., 2007; Peng et al., 2019). A fluctuation in the density is observed near the fiber center also reported in previous studies (Curgul et al., 2007; Buell et al., 2009; Peng et al., 2019) which results from poorer statistical sampling for shells with a small radius, however, it does not affect our conclusions.

It is important to set up a method to calculate the radius of nanofibers; The value of stress and subsequently the mechanical parameters are affected by the considered value for the cross-section (as will be addressed in Section 2.6). Also, the glass transition temperature (Tg) and coefficient of thermal expansion (CTE) are calculated by tracking the change of radius versus temperature (as will be explained in Section 2.5). The available studies on coarse-grained MD simulation of PNFs have usually used the Gibbs dividing surface (GDS) method based on the radial density profile (Curgul et al., 2007; Buell et al., 2009, 2010; Deng et al., 2017). In a simplified expression, GDS for nanofibers determines the radius of a homogenous fiber with a density equal to the fiber core and with the same integral mass of the original fiber. In the current study, we used another criterion for the effective radius that exhibits much less noise during uniaxial deformation in comparison to the radii

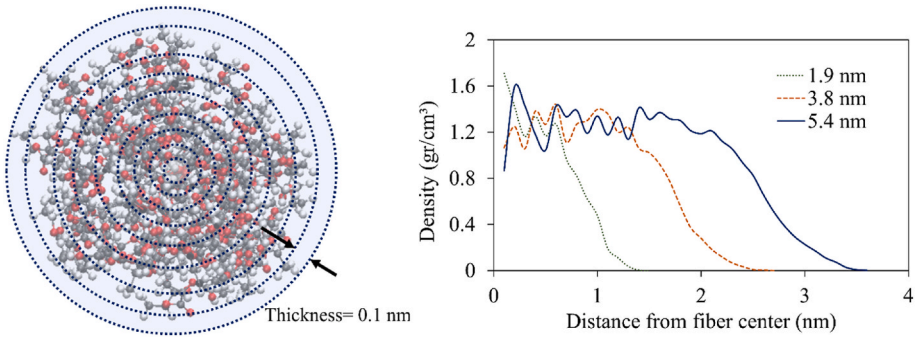

Fig. 4. a) Schematic of nanofibers cross-sections divided into concentric cylindrical shells of 0.1 nm thickness. b) Distribution of radial mass density of nanofibers with different effective radii.

obtained from GDS. In this method, the radial distance (R_i) of all atoms from the centroid is calculated and averaged at each time step and the average has set equal to the mean radius (R_{ave}) of an equivalent solid circle. The radius of the equivalent cylinder is deemed as the effective radius (R_{eff}) of nanofibers considering $2R_{eff}/3 = R_{ave}$ as explained through Eq. (2). The method is illustrated in Fig. 5;

$$\frac{\int_A r\, dA}{\pi {R_{eff}}^2} = \frac{2R_{eff}}{3} = R_{ave} \tag{2}$$

Through this procedure, the initial R_{eff} for the three studied nanofibers are 1.92 nm, 3.8 nm and 5.4 nm.

2.5. Glass transition temperature and coefficient of thermal expansion

The glass transition temperature is an important feature in polymeric materials delimiting the glassy regime to the rubbery one (Hossain et al., 2010; Capaldi et al., 2004). Since polymer in the rubbery and glassy regimes possesses different thermal expansion coefficients, the slope of the specific volume versus temperature curve changes upon crossing Tg. To find the Tg of nanofibers, the specific volume which is directly related to the effective radius is monitored while the temperature of the equilibrated nanofiber is cooled down from 500 K to 1 K with a cooling rate of 0.5K/ps under the NVT ensemble. The intersection of fitted linear lines from the two sides gives Tg (Fig. 6). For the bulk polymer, Tg is determined with the same procedure but under the NPT ensemble.

Due to the free lateral surface, the slope of the effective radius with respect to temperatures determines the coefficient of thermal expansions in both glassy and rubbery states (Eq. (3)).

$$\Delta R_{eff} = \alpha_{CTE}\, R_{eff0} \Delta T \tag{3}$$

Where α_{CTE} is the radial coefficient of thermal expansion, R_{eff0} is the initial effective radius at each phase, T denotes the temperature and Δ signs the difference.

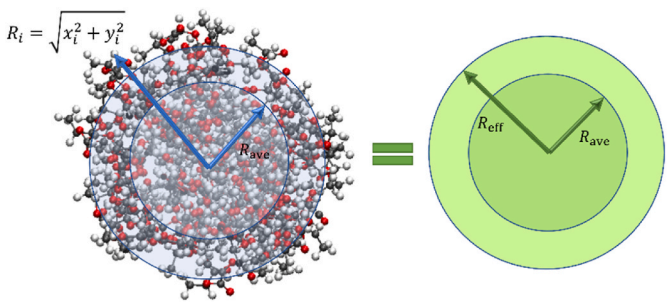

Fig. 5. Determination of effective radius.

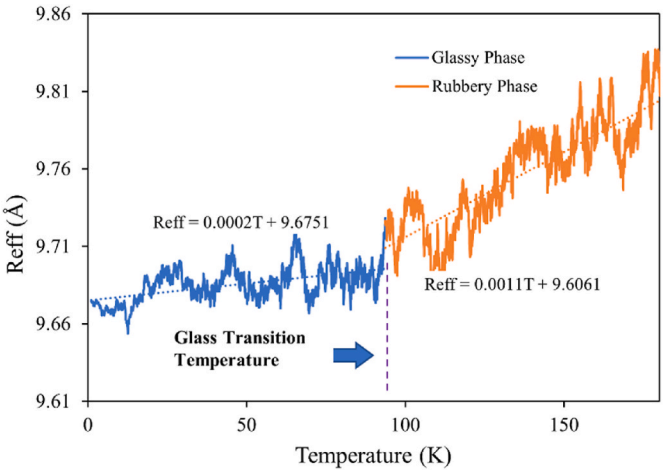

Fig. 6. The change of R_{eff} versus temperature for PNF with 1.93 nm initial diameter - glass transition temperature and radial coefficient of thermal expansion can be determined from the curve.

2.6. Tensile behaviour

After equilibrating nanofibers, while keeping the temperature constant through Langevin thermostat, a uniaxial deformation with a constant strain rate is applied on each nanofiber by uniformly changing the box size in the fiber's axial direction. As the lateral surface is unconstrained, the deformation resembles a uniaxial tensile test. The stress tensors are calculated using the Virial theorem (Tsai, 1979), However, in LAMMPS the applied volume in Virial stress is the volume of the simulation box, thus the obtained stresses are corrected by the ratio of the simulation box to the fiber volume using the effective radius defined in Section 2.4.

Through the stress-strain curve, Young's modulus is determined using the slope of the linear elastic regime (Fig. 7a) and the Poisson's ratio is obtained by monitoring the radial deformation in the same regime (Fig. 7c). Besides the yield stress, the post-yield behaviour is analyzed from which toughness fracture properties are characterized. Fig. 7b depicts the structural evolution of the nanofiber with a 5.4 nm diameter during tensile deformation. To reduce the noise on the stress data, especially at higher temperatures, a regression with the smooth function in MATLAB using a moving average filter is applied.

In addition to stress calculation, the strain energy is tracked as a function of strain which is useful in the determination of fracture toughness. The dependence of mechanical response on the nanofiber diameter, strain rate and temperature is studied. The procedure is repeated and averaged for three initial configurations. Three different temperatures are examined; 0.01 Tg in which the effect of temperature is minimized to enable better structural comparison of nanofibers and two

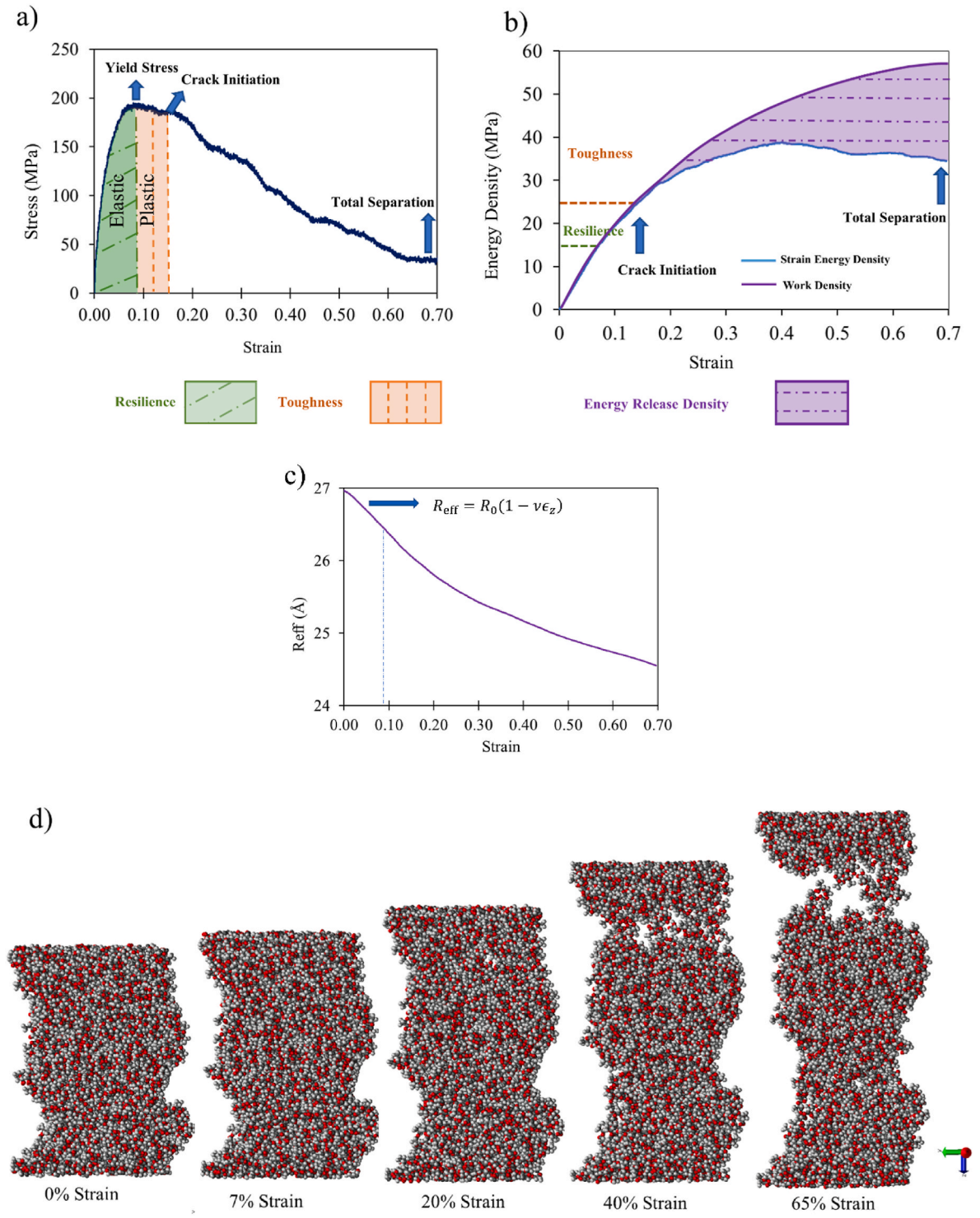

Fig. 7. a) Stress-strain response of glassy polymer nanofiber with 5.4 nm diameter deformed in uniaxial tension at strain rate of 10^8/s and temperature of 0.01 Tg. b) Evolution of strain energy and work densities c) Effective radius versus strain d) Nanofiber structures at different strains until fracture.

other temperatures 0.4 and 0.8 Tg.

For the sake of comparison, the mechanical properties of the RVE representing the bulk state are also determined under a uniaxial tensile test using NPT ensemble where a zero-pressure condition is applied on the lateral faces with a constant strain rate of 10^8 1/s in the z-direction. The moduli of resilience and toughness are the area under the stress-strain curve until the yield and crack onset, respectively. They represent the amount of strain energy per volume a material can accommodate before yielding or fracture takes place. In the current work, instead of calculating the under-curve area, the potential energy is directly utilized to obtain strain energy density ($\frac{\text{Potential energy} - \text{initial potential energy}}{\text{nanofiber volume}}$) at these two critical loci (Fig. 7b).

3. Results and discussion

3.1. Stress-strain curve

The isothermal stress-strain of a typical PLA nanofiber with 5.4 nm is

shown in Fig. 7a. The curve is partitioned into 4 regimes; elastic, yield, softening and fracture. The stress first increases linearly proportional to the applied strain evidencing an elastic regime. Further increase in the strain decreases the stress-strain slope until local flattening of the curve indicating the yield point. Upon this point, the material experience a strain softening regime due to slippage of the polymer chains. Some local maximums are also observed in the post-yield region. These local maximums are attributed to the alignment of polymer chains to the applied strain direction. This phenomenon causes strain hardening in bulk polymers (Hossain et al., 2010; Capaldi et al., 2002, 2004), whereas, for current nanofibers, only local stiffness increases are observed.

By further loading, the polymer chains initiate to pull out slightly of each other calling crack initiation. Upon this point, a sensible decrease in the stress diagram along with a slight increase in the fluctuation of the strain energy curve is observed. However, crack initiation can be better distinguished by monitoring the difference between the applied work and the strain energy as will be detailed in Section 3.2. Finally, when the total separation occurs, the stress magnitude remains constant, thereafter. Monitoring the structural evolution of nanofiber during loading confirms the above interpretations (Fig. 7d). As observed in Fig. 7d, atoms configuration forms some rippling on the surface of equilibrated nanofiber which is consistent with available SEM images (Tang et al., 2014), however, it may also be the frozen configurations due to fast cooling rate.

It should be noted that even in the undeformed nanofibers there exists an initial stress, i.e., a nonzero stress when the strain magnitude is zero, which is consistent with the literature and is attributed to the surface tension of the nanofibers (Buell et al., 2009; Kwon and Sung, 2020). In all the stress-strain figures in the current work, this initial stress is subtracted.

3.2. Energy release rate

The energy release rate (G) is a fundamental parameter in fracture mechanics quantified by the amount of energy release per unit area of the growing fractured surface as the crack propagates.

$$G = -\frac{\Delta(U - W_{ext})}{\Delta A_{crack}} \tag{4}$$

where W_{ext} and U are the external work and the stored strain energy, respectively and A_{crack} is the cracked area. In the current study, $W_{ext} = \int_0^l F dl$, calculated through the integration of an interpolation function for force (F)-displacement (l) data using "*griddedInterpolant*" MATLAB function. The strain energy is obtained by instant potential energy subtracted by its initial value.

As shown in Fig. 7b, prior to crack initiation, all the work done on the nanofiber is stored as the strain energy. However, where the polymer chains start to pull out, which we donate as crack emergence, a growing difference arises between W_{ext} and U associated with the energy release due to chain separations. As illustrated in Fig. 8, considering A_{crack} equal to zero where the crack initiates and equal to the nanofiber area where the total separation occurs, the slope of $W_{ext} - U$ versus A_{crack} determines the energy release rate. The determined values for G, the strains at which the crack initiates and becomes critical are listed in Table 1 for different nanofiber diameters.

3.3. Internal energy evolution

To gain a better insight into the deformation mechanism in the regimes of elastic, yield, softening and fracture, the individual components of energy are tracked as a function of applied strain which constitutes the bonding energy, the bond angle energy, the dihedral energy and non-bonded energy (Fig. 9). For the sake of comparison, the components are normalized by their initial value.

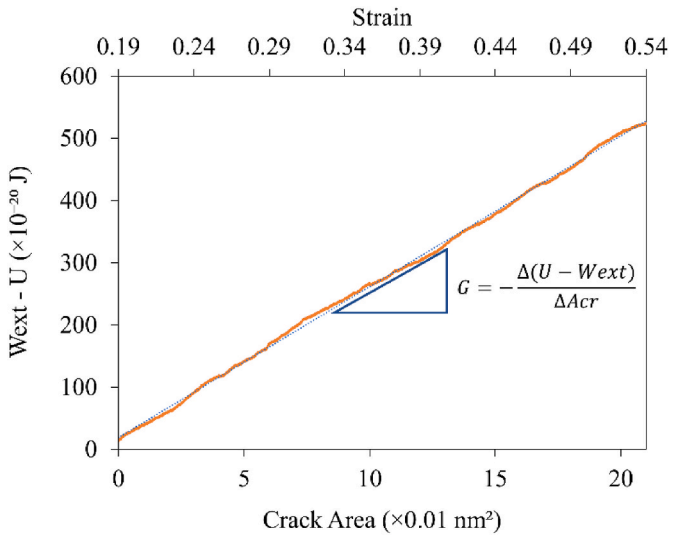

Fig. 8. Energy release rate for PLA nanofiber with 5.4 nm diameter at 0.01 Tg for a strain rate of 10^8 1/s.

As inferred from Fig. 9, the deformation is mainly dominated by contributions of bond and van der Waals energies. The van der Waals energy decreases sharply during the deformation because the atoms move continuously away from each other. In the elastic region, the bond energy decreases monotonically; this could be due to the fact that the bonds in the curved polymer chains are far from their equilibrium length and approach the equilibrium value by stretching the chains during deformation. This observation is consistently reported in (Hossain et al., 2010) from MD simulations of polyethylene in the bulk state. Upon yielding, the bond energy stays constant while the van der Waals term decreases steadily which can be correlated to the chain slippage mechanism. Further loading untangles the polymer chains and they start to pull out of each other, this alters the bond energy level as the stretch in the nanofiber initiates to relax and the slope of the van der Waals curve is also affected at this juncture. After complete separation, the bond energy related to the elastic deformation is retained, while the energy due to plastic deformation associated with the change in the chain alignment persists and the van der Waals energy gets constant.

3.4. Diameter dependence

In this Section, the dependence of PNFs' tensile properties on the diameter is studied. As shown in Fig. 10 and Table 1, increasing diameter slightly improves Young's modulus whereas reduces Poisson's ratio which implies that PNFs with larger diameters are stiffer but more compressible. The above observation is associated with the surface layer which has a lower density compared to the core. Since the stiffness of a polymer is directly related to its density (Holliday and White, 1971; Weishaupt et al., 1995; Izadi et al., 2021), the surface layer is less stiff than the core region; however, as the thickness of this layer is almost constant, its effect is reduced by increasing the PNF diameter. The increasing trend of PNFs Young's modulus for polyethylene nanofibers is consistently reported in the literature (Buell et al., 2009; Tang et al., 2014) using the coarse grain-MD simulations as presented in Fig. 10b.

It should be noted that although the fabrication of very fine nanofibres (down to 0.17 nm diameter (Jian et al., 2018)) is reported in literature, no experimental data are available for the diameter range studied in the current work. This is due to the difficulties associated with mechanical testing at very fine diameters, such as mounting and anchoring the nanofibers on micro ridges to avoid slippage, exerting nano-force in the proper position, and providing loadcells with extremely high sensitivity (Jahanmard-Hosseinabadi et al., 2018; Neugirg et al., 2016). This limitation, also pointed out by Buell et al. (2009),

Table 1
Thermomechanical parameters of PLA nanofibers with different diameters, temperatures, and strain rates.

Fiber Diameter at 1 K (nm)	Strain Rate (1/s)	Temperature (K)	Young's modulus (GPa)	Poisson's ratio	Proportional Stress (MPa)	Yield Stress (MPa)	Resilience (MPa)	Toughness (MPa)	Energy Release Rate (mJ/m^2)	Tg (K)	CTE ($\times 10^{-5}$ 1/K)
1.92	10^8	0.01 Tg	2.7	0.26	96	137	18.20	24.59	175	92	2.25
	10^9	0.01 Tg	4.4	0.14	248	332	30.08	43.09	842		
	10^{10}	0.01 Tg	8.3	0.04	684	812	53.30	76.35	2921		
3.8	10^8	0.01 Tg	3.7	0.22	109	160	22.33	26.98	218	115	6.55
5.4	10^8	0.01 Tg	4.1	0.19	133	178	14.78	29.75	242	125	6.83
		0.4 Tg	3.7	0.22	133	170	11.39	21.85	200		
		0.8 Tg	1.1	0.23	54	72	8.86	19.37	125		
Bulk	10^8	0.01 Tg	5.7	0.33	287	287	7.32	60.34	347	127	6.55

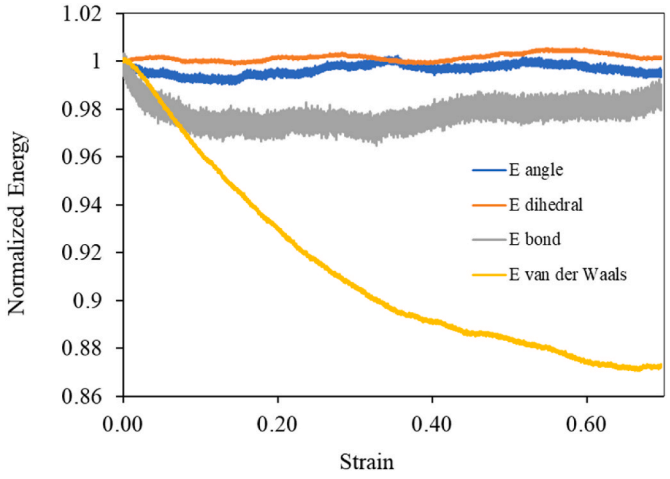

Fig. 9. Energy decomposition for PLA nanofiber with 5.4 nm diameter at 0.01 Tg for a strain rate of 10^8 1/s. The non-bonded energy decreases sharply throughout deformation, the bond energy changes drastically during the elastic region with less significant contribution of angle and dihedral energies.

in turn justifies the use of atomistic simulation for this range of small diameter nanofibres.

Nonetheless, we can consider the characteristics of bulk PLA as a comparison of MD simulation results with known experiments. The obtained Young's modulus and tensile stress for the bulk state are 5.7 GPa and 287 MPa, respectively, which are within the reported ranges for PLA in experiments, which are 3.9–8.6 GPa for Young's modulus and 70–880 MPa for tensile stress (Farah et al., 2016; Auras et al., 2011).

The smaller Poisson's ratio for larger diameters, as a sign of more compressibility, is consistent with the observation of Tang et al. (2014) in which through MD simulation and FEM calculation a especial focus is devoted to the role of Poisson's ratio on nanofiber configurations.

In Fig. 11, the mechanical parameters for different diameters are normalized to the corresponding value of the polymer bulk. All the mechanical parameters of nanofibers, except for Poisson's ratio and resilience, increase monotonically by the diameter attributed to the decrease in the volume fraction of the surface layer in larger diameters.

3.5. Temperature dependence

In Fig. 12, the influence of temperature on the stress-strain properties of nanofibers is illustrated for a typical nanofiber with a strain rate of 10^8 1/s considering three cases; 0.8 Tg, 0.4 Tg and 0.01 Tg.

According to Fig. 12 and Table 1, when the temperature changes from 0.01 Tg to 0.4 Tg, the stress-strain response is slightly affected, however, the temperature effect increases when it approached Tg. By raising the temperature, the nanofibers exhibit more ductility; Young's modulus, proportional and yield stresses, moduli of resilience and toughness and energy release rate decrease, however, the yield and

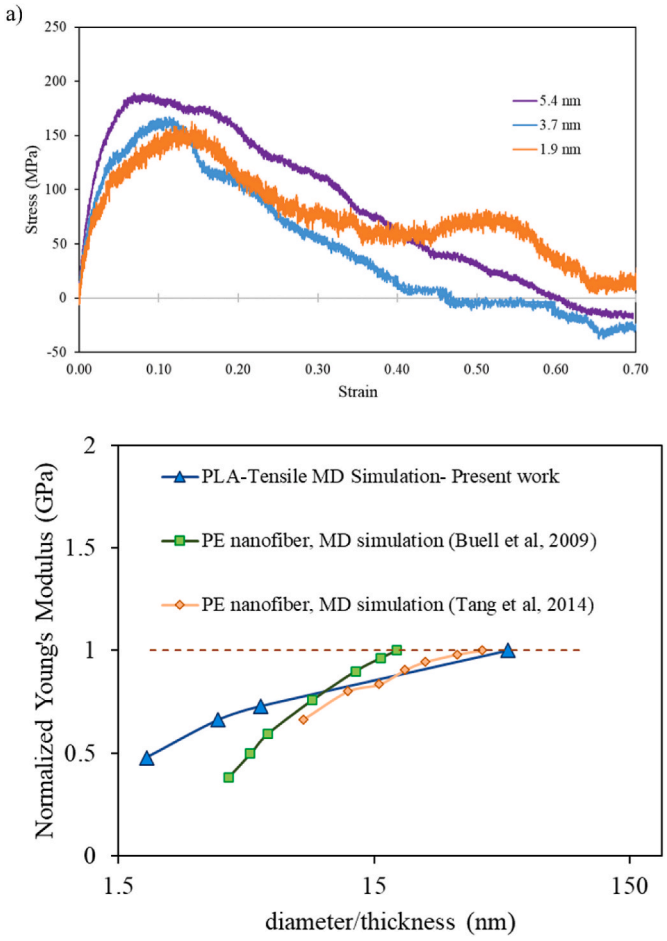

Fig. 10. a) Stress strain response for different PNF diameters b) The Size-dependency in the normalized Young's modulus of nanofibers obtained from MD simulations (Buell et al., 2009; Tang et al., 2014).

fracture slow down and occur at higher strains. In addition, Poisson's ratio increases which shows the reduction in compressibility.

3.6. Strain rate dependence

The effect of strain rate on tensile properties is illustrated in Fig. 13 where a PNF with 1.9 nm diameter is deformed under three strain rates of 10^8 1/s, 10^9 1/s and 10^{10} 1/s. As shown in Fig. 13 and Table 1, the variation between stress-strain curves with different strain rates possess similar overall trends and regimes, however, as the strain rate increases, the material exhibit more brittleness; The magnitudes of Young's modulus and yield stress, moduli of toughness and resilience as well as the energy release rate increase while the Poisson's ratio decreases.

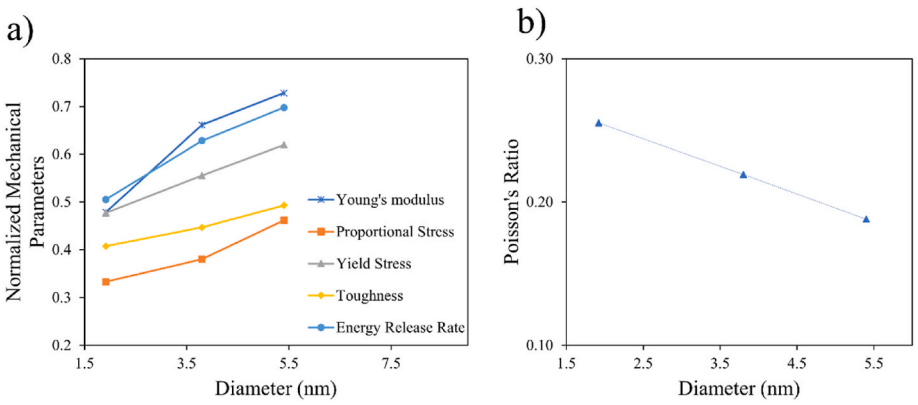

Fig. 11. a) Normalized mechanical parameters of PNFs with different diameters to the bulk parameters b) Poisson's ratio of PNFs with different diameters.

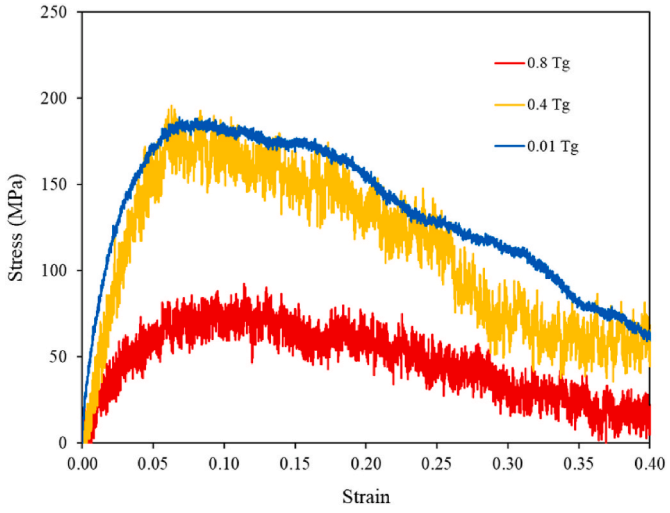

Fig. 12. Stress strain response for PLA nanofiber with 5.4 nm diameter for different temperatures at strain rates of 10^8 1/s.

However, yielding and fracture strains are almost independent of the strain rate although the strain at proportional limit approaches the yield stress as a sign of more brittleness. Although not shown in Fig. 13, in all three strain rates, after the complete separation, the axial stress finally relaxes back to around the initial value, however, for higher strain rates, the relaxation lingers.

3.7. Glass transition temperature and coefficient of thermal expansion

The glass transition temperature and coefficient of thermal expansion of the three nanofibers with different cross sections are determined by the method described in Section (2.5) and illustrated in Fig. 14 by normalizing Tgs and CTEs to that of bulk polymer. As shown in Fig. 14. a Tg of PNFs are lower, yet rapidly approaching Tg of the bulk is consistent with literature (Curgul et al., 2007; Richard-Lacroix and Pellerin, 2012; Wang and Barber, 2012) and associated with higher mobility in the surface region. Focusing on CTEs, the surface tension hinders nanofibers to expand in the radial direction in both glassy and rubbery phases, however; as PNF becomes larger and the surface region loses its dominancy, CTE of PNFs approaches bulk CTE very quickly.

The amount of CTE of bulk is 6.5×10^{-5} which is in good agreement with experiment (4–8.5 $\times$ 10^{-5} (Lim et al., 2008; Wijnen et al., 2018) (Kuciel et al., 2020; Technical Data Sheet PLA, 2022)). In the current work, PLA with low-molecular-weight (1458 amu) is simulated for the sake of calculation and to better monitor the interchain behaviour under loading. The Tg the PLA bulk modulus with this molecular weight is 127 K which is smaller than the experimentally obtained Tg (around 300 K) for PLA with the high-molecular weight of 2×10^4 amu. However, the obtained value for Tg is consistent with the prediction of the Fox–Flory curve. Fox-Flory equation is a verified relation indicating the dependence of Tg on the number-average molecular weights.

$$Tg(Mw) = T_{g,\infty} - K_g / Mw \tag{6}$$

where $T_{g,\infty}$ is the limiting value of the glass transition temperature at very high molecular weight, Mw is the number-average molecular

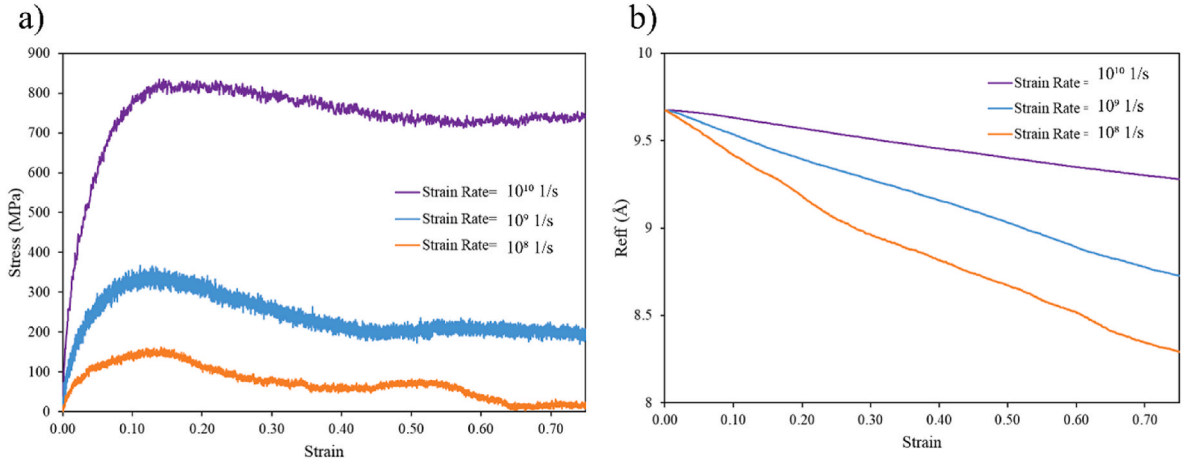

Fig. 13. a) Stress strain response and b) evolution of R_{eff} for PLA nanofiber with 1.93 nm diameter at 1 K for different strain rates.

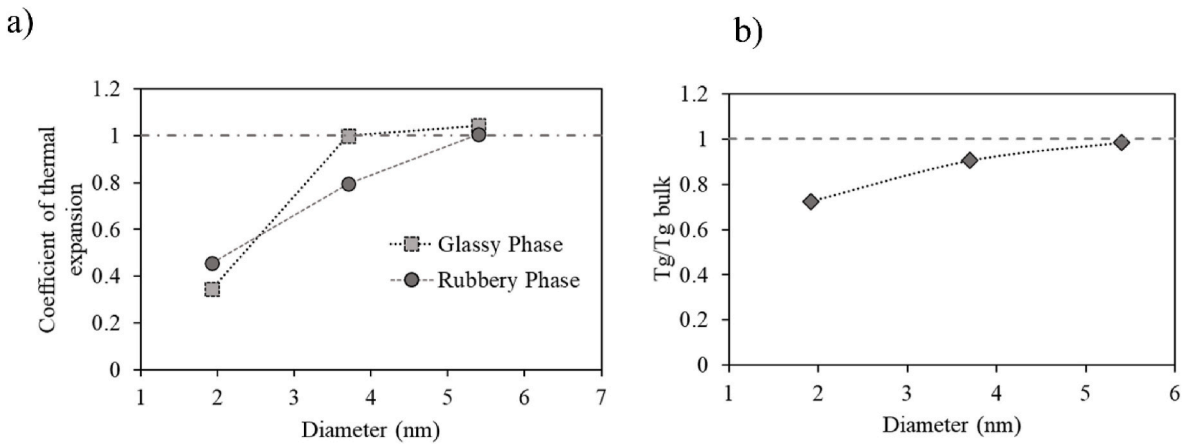

Fig. 14. a) CTE of PNFs in both glassy and rubbery phases approaches bulk CTE very quickly. b) Tg of PNFs vs diameter.

weight and K is a constant for a given polymer. According to the experimental work of Dorgan and co-workers (Dorgan et al., 2005), the values of $T_{g,\infty}$ and K_g for PLA are estimated as 54.6–56.5 K and 2.7 × 10^4–3 × 10^4 amu, respectively. Based on these data, the obtained Tg for the molecular weight of the current work will be 123–142 K which is consistent with the obtained results.

4. Summary and conclusion

The growing and diverse applications of polymer nanofibers prompt endeavors to deepen our cognition of their physical properties. Special attention is devoted to biodegradable nanofibers such as PLA due to their bio-friendly and peculiar applications in different areas of science like tissue engineering, nanocomposites, wound covering, sensors, and filtration and other disciplines.

The current paper aims at elucidating the tensile mechanism of PLA nanofibers using all-atom molecular dynamics simulations from which various thermomechanical parameters are determined.

- The simulated-tensile test encompasses all the elastic, yield, post-yield and fracture phases where different mechanical parameters are evaluated tracking the stress-strain curve, strain energy and geometrical evolutions during loading.
- A criterion is proposed to determine the effective radius for nanofibers, whose variation during the elastic phase quantifies the Poisson's ratio.
- Monitoring the external work and strain energy stored in the nanofibers during tensile loading provides information on the onset of crack initiation and propagation. The deviation of the external work from the stored energy announces crack initiation during static loading. The difference under further loading determines the energy release rate of PNFs, which is an important factor in fracture mechanics and is studied for the first time in the literature on PNFs.
- Scanning of radial density profiles in nanofibers confirms the presence of a cylindrical surface layer responsible for the size-dependent thermomechanical behaviour of PLA nanofibers. When the diameter increases and the surface layer is inferior to the core region, PLA nanofibers are mechanically improved, as evidenced by an increase in Young's modulus, yield stress, resilience, toughness, and energy release rate. In addition, the increase in Poisson's ratio at smaller diameters is indicative of higher incompressibility due to the dominant presence of the surface layer.
- The deformation mechanism is unraveled by simultaneously monitoring the stress, energy components, and structural evolution during loading. The deformation is dominated mainly by the contributions of bond and van der Waals energies.

Author contribution

Razie Izadi: Conceptualization, Methodology, Software, Data curation, Writing- Original draft preparation, Visualization, Investigation. **Meral Tuna:** Conceptualization, Methodology, Writing- Reviewing and Editing **Patrizia Trovalusci:** Conceptualization, Supervision, Resources, Funding acquisition, Writing- Reviewing and Editing **Nicholas Fantuzzi:** Conceptualization, Methodology, Writing- Reviewing and Editing.

Funding

This work was supported by Italian Ministry of University and Research [no. 1062 of August 10, 2021, the endowment of the PON "Research and Innovation" 2014–2020]; PRIN 2017, project 2017HFPKZY [grant number B86J16002300001]; PRIN 2020, project 2020F23HZ7_003 [grant number J35F22000640001] and Progetto Grande di Ateneo bando 2021 [grant number B85F21008380001].

Declaration of competing interest

The authors declare that they have no known competing financial interests or personal relationships that could have appeared to influence the work reported in this paper.

Data availability

Data will be made available on request.

References

Abdal-hay, A., Sheikh, F.A., Lim, J.K., 2013. Air jet spinning of hydroxyapatite/poly (lactic acid) hybrid nanocomposite membrane mats for bone tissue engineering. Colloids Surf. B Biointerfaces 102, 635–643.
Abdal-Hay, A., et al., 2016. Fabrication of novel high performance ductile poly (lactic acid) nanofiber scaffold coated with poly (vinyl alcohol) for tissue engineering applications. Mater. Sci. Eng. C 60, 143–150.
Agarwal, S., Wendorff, J.H., Greiner, A., 2009. Progress in the field of electrospinning for tissue engineering applications. Adv. Mater. 21 (32-33), 3343–3351.
Ajayan, P.M., Schadler, L.S., Braun, P.V., 2006. Nanocomposite Science and Technology. John Wiley & Sons.
Andreopoulos, A., Hatzi, E., Doxastakis, M., 2000. Controlled release systems based on poly (lactic acid). An in vitro and in vivo study. J. Mater. Sci. Mater. Med. 11 (6), 393–397.
Auras, R.A., et al., 2011. Poly (Lactic Acid): Synthesis, Structures, Properties, Processing, and Applications, vol. 10. John Wiley & Sons.
Baker, S.R., et al., 2016. Determining the mechanical properties of electrospun poly-ε-caprolactone (PCL) nanofibers using AFM and a novel fiber anchoring technique. Mater. Sci. Eng. C 59, 203–212.
Bergsma, J.E., et al., 1995. Late degradation tissue response to poly (L-lactide) bone plates and screws. Biomaterials 16 (1), 25–31.

BIOVIA, D.S., 2017. Materials Studio. Available from: https://www.3ds.com/products-services/biovia/.
Blasi, P., 2019. Poly (lactic acid)/poly (lactic-co-glycolic acid)-based microparticles: an overview. J. Pharm. Investigation 49, 337–346.
Buell, S., Van Vliet, K.J., Rutledge, G.C., 2009. Mechanical properties of glassy polyethylene nanofibers via molecular dynamics simulations. Macromolecules 42 (13), 4887–4895.
Buell, S., Rutledge, G.C., Vliet, K.J.V., 2010. Predicting polymer nanofiber interactions via molecular simulations. ACS Appl. Mater. Interfaces 2 (4), 1164–1172.
Bussi, G., Zykova-Timan, T., Parrinello, M., 2009. Isothermal-isobaric molecular dynamics using stochastic velocity rescaling. J. Chem. Phys. 130 (7), 074101.
Capaldi, F.M., Boyce, M.C., Rutledge, G.C., 2002. Enhanced mobility accompanies the active deformation of a glassy amorphous polymer. Phys. Rev. Lett. 89 (17), 175505.
Capaldi, F.M., Boyce, M.C., Rutledge, G.C., 2004. Molecular response of a glassy polymer to active deformation. Polymer 45 (4), 1391–1399.
Carlisle, C.R., et al., 2009. The mechanical properties of individual, electrospun fibrinogen fibers. Biomaterials 30 (6), 1205–1213.
Carlisle, C.R., Coulais, C., Guthold, M., 2010. The mechanical stress–strain properties of single electrospun collagen type I nanofibers. Acta Biomater. 6 (8), 2997–3003.
Chen, S., et al., 2012. The influence of fiber diameter of electrospun poly (lactic acid) on drug delivery. Fibers Polym. 13 (9), 1120–1125.
Chew, S.Y., et al., 2006. Mechanical properties of single electrospun drug-encapsulated nanofibres. Nanotechnology 17 (15), 3880.
Curgul, S., Van Vliet, K.J., Rutledge, G.C., 2007. Molecular dynamics simulation of size-dependent structural and thermal properties of polymer nanofibers. Macromolecules 40 (23), 8483–8489.
Deng, S., Arinstein, A., Zussman, E., 2017. Size-dependent mechanical properties of glassy polymer nanofibers via molecular dynamics simulations. J. Polym. Sci. B Polym. Phys. 55 (6), 506–514.
Ding, B., et al., 2009. Gas sensors based on electrospun nanofibers. Sensors 9 (3), 1609–1624.
Dorgan, J.R., et al., 2005. Melt rheology of variable L-content poly (lactic acid). J. Rheol. 49 (3), 607–619.
Engler, A.J., et al., 2006. Matrix elasticity directs stem cell lineage specification. Cell 126 (4), 677–689.
Farah, S., Anderson, D.G., Langer, R., 2016. Physical and mechanical properties of PLA, and their functions in widespread applications—a comprehensive review. Adv. Drug Deliv. Rev. 107, 367–392.
Garlotta, D., 2001. A literature review of poly (lactic acid). J. Polym. Environ. 9 (2), 63–84.
Gopal, R., et al., 2006. Electrospun nanofibrous filtration membrane. J. Membr. Sci. 281 (1–2), 581–586.
Guhados, G., Wan, W., Hutter, J.L., 2005. Measurement of the elastic modulus of single bacterial cellulose fibers using atomic force microscopy. Langmuir 21 (14), 6642–6646.
Han, C., et al., 2018. Enhanced drug delivery, mechanical properties and antimicrobial activities in poly (lactic acid) nanofiber with mesoporous Fe3O4-COOH nanoparticles. Colloids Surf. A Physicochem. Eng. Asp. 559, 104–114.
Hasheminejad, K., Montazeri, A., 2020. Enhanced interfacial characteristics in PLA/graphene composites through numerically-designed interface treatment. Appl. Surf. Sci. 502, 144150.
Holliday, L., White, J., 1971. The stiffness of polymers in relation to their structure. Pure Appl. Chem. 26 (3–4), 545–582.
Hossain, D., et al., 2010. Molecular dynamics simulations of deformation mechanisms of amorphous polyethylene. Polymer 51 (25), 6071–6083.
Huang, Z.-M., et al., 2003. A review on polymer nanofibers by electrospinning and their applications in nanocomposites. Compos. Sci. Technol. 63 (15), 2223–2253.
Huang, C., et al., 2006. Electrospun polymer nanofibres with small diameters. Nanotechnology 17 (6), 1558.
Izadi, R., Ghavanloo, E., Nayebi, A., 2019. Elastic properties of polymer composites reinforced with C60 fullerene and carbon onion: molecular dynamics simulation. Phys. B Condens. Matter 574, 311636.
Izadi, R., Nayebi, A., Ghavanloo, E., 2021. Combined molecular dynamics–micromechanics methods to predict Young's modulus of fullerene-reinforced polymer composites. Eur. Phys. J. Plus 136 (8), 816.
Jabbari, E., He, X., 2008. Synthesis and characterization of bioresorbable in situ crosslinkable ultra low molecular weight poly (lactide) macromer. J. Mater. Sci. Mater. Med. 19, 311–318.
Jahanmard-Hosseinabadi, F., Amani-Tehran, M., Eslaminejad, M.B., 2018. Mathematical Modeling and Experimental Evaluation for the predication of single nanofiber modulus. J. Mech. Behav. Biomed. Mater. 79, 38–45.
Jayaraman, K., et al., 2004. Recent advances in polymer nanofibers. J. Nanosci. Nanotechnol. 4 (1–2), 52–65.
Jian, S., et al., 2018. Nanofibers with diameter below one nanometer from electrospinning. RSC Adv. 8 (9), 4794–4802.
Klotz, S., et al., 2016. Biotechnological production of enantiomerically pure d-lactic acid. Appl. Microbiol. Biotechnol. 100 (22), 9423–9437.
Kuciel, S., Mazur, K., Hebda, M., 2020. The influence of wood and basalt fibres on mechanical, thermal and hydrothermal properties of PLA composites. J. Polym. Environ. 28 (4), 1204–1215.
Kwon, T., Sung, B.J., 2020. Confinement effects on the mechanical heterogeneity of polymer fiber glasses. Phys. Rev. 102 (5), 052501.
Lannutti, J., et al., 2007. Electrospinning for tissue engineering scaffolds. Mater. Sci. Eng. C 27 (3), 504–509.
Li, Y., Wan, W., 2017. Exploring Polymer Nanofiber Mechanics: a review of the methods for determining their properties. IEEE Nanotechnol. Magazine 11 (3), 16–28.
Lim, L.-T., Auras, R., Rubino, M., 2008. Processing technologies for poly (lactic acid). Prog. Polym. Sci. 33 (8), 820–852.
Liu, H., et al., 2021. Insights into the tensile behavior of polymer nanofibers with hierarchically twisted chains. Comput. Mater. Sci. 194, 110463.
Maleki, H., et al., 2022. Poly (lactic acid)-based electrospun fibrous structures for biomedical applications. Appl. Sci. 12 (6), 3192.
Marrink, S.J., et al., 2007. The MARTINI force field: coarse grained model for biomolecular simulations. J. Phys. Chem. B 111 (27), 7812–7824.
Martinez, G.A., et al., 2011. A computer tool for the development of poly (lactic acid) synthesis process from renewable feedstock for biomanufacturing. In: Computer Aided Chemical Engineering. Elsevier, pp. 346–350.
Milani, A., et al., 2011. Coarse-grained simulations of model polymer nanofibres. Macromol. Theory. Simul. 20 (5), 305–319.
Mohammadzadehmoghadam, S., Dong, Y., Davies, I.J., 2016. Modeling electrospun nanofibers: an overview from theoretical, empirical, and numerical approaches. Int. J. Polymeric Mater. Polymeric Biomater. 65 (17), 901–915.
Neugirg, B.R., et al., 2016. AFM-based mechanical characterization of single nanofibres. Nanoscale 8 (16), 8414–8426.
Peng, C., Zeng, F., 2017. A molecular simulation study to the deformation Behaviors and the size effect of polyethylene during nanoindentation. Comput. Mater. Sci. 137, 225–232.
Peng, K., Nain, A., Mirzaeifar, R., 2019. Tracking the origins of size dependency in the mechanical properties of polymeric nanofibers at the atomistic scale. Polymer 175, 118–128.
Place, E.S., Evans, N.D., Stevens, M.M., 2009. Complexity in biomaterials for tissue engineering. Nat. Mater. 8 (6), 457–470.
Prasitnok, K., 2016. A coarse-grained model for polylactide: glass transition temperature and conformational properties. J. Polym. Res. 23 (7), 1–9.
Rao, N., et al., 2013. A co-culture device with a tunable stiffness to understand combinatorial cell–cell and cell–matrix interactions. Integr. Biol. 5 (11), 1344–1354.
Richard-Lacroix, M., Pellerin, C., 2012. Orientation and structure of single electrospun nanofibers of poly (ethylene terephthalate) by confocal Raman spectroscopy. Macromolecules 45 (4), 1946–1953.
Sagadevan, S., Periasamy, M., 2014. Recent trends in nanobiosensors and their applications-a review. Rev. Adv. Mater. Sci. 36, 62–69, 2014.
Santoro, M., et al., 2016. Poly (lactic acid) nanofibrous scaffolds for tissue engineering. Adv. Drug Deliv. Rev. 107, 206–212.
Sarapirom, S., et al., 2014. Effect of surface modification of poly (lactic acid) by low-pressure ammonia plasma on adsorption of human serum albumin. Appl. Surf. Sci. 310, 42–50.
Scaffaro, R., et al., 2017. Polysaccharide nanocrystals as fillers for PLA based nanocomposites. Cellulose 24, 447–478.
Scaffaro, R., Maio, A., Nostro, A., 2020. Poly (lactic acid)/carvacrol-based materials: preparation, physicochemical properties, and antimicrobial activity. Appl. Microbiol. Biotechnol. 104, 1823–1835.
Schneider, T., Stoll, E., 1978. Molecular-dynamics study of a three-dimensional one-component model for distortive phase transitions. Phys. Rev. B 17 (3), 1302.
Sonseca, Á., Menes, O., Giménez, E., 2017. A comparative study of the mechanical, shape-memory, and degradation properties of poly (lactic acid) nanofiber and cellulose nanocrystal reinforced poly (mannitol sebacate) nanocomposites. RSC Adv. 7 (35), 21869–21882.
Stevens, M.M., George, J.H., 2005. Exploring and engineering the cell surface interface. Science 310 (5751), 1135–1138.
Sun, H., 1994. Force field for computation of conformational energies, structures, and vibrational frequencies of aromatic polyesters. J. Comput. Chem. 15 (7), 752–768.
Sun, H., 1995. Ab initio calculations and force field development for computer simulation of polysilanes. Macromolecules 28 (3), 701–712.
Sun, H., et al., 1994. An ab initio CFF93 all-atom force field for polycarbonates. J. Am. Chem. Soc. 116 (7), 2978–2987.
Taib, N.-A.A.B., et al., 2022. A review on poly lactic acid (PLA) as a biodegradable polymer. Polym. Bull. 1–35.
Tang, S., et al., 2014. Surface ripples of polymeric nanofibers under tension: the crucial role of Poisson's ratio. Macromolecules 47 (18), 6503–6514.
Technical Data Sheet PLA (poly lactic acid) Available from: https://www.sd3d.com/3d-printing/materials/.
Thompson, A.P., et al., 2022. LAMMPS-a flexible simulation tool for particle-based materials modeling at the atomic, meso, and continuum scales. Comput. Phys. Commun. 271, 108171.
Tsai, D., 1979. The virial theorem and stress calculation in molecular dynamics. J. Chem. Phys. 70 (3), 1375–1382.
Tsuji, H., 2005. Poly (lactide) stereocomplexes: formation, structure, properties, degradation, and applications. Macromol. Biosci. 5 (7), 569–597.
Tyler, B., et al., 2016. Polylactic acid (PLA) controlled delivery carriers for biomedical applications. Adv. Drug Deliv. Rev. 107, 163–175.
Vao-soongnern, V., Doruker, P., Mattice, W.L., 2000. Simulation of an amorphous polyethylene nanofiber on a high coordination lattice. Macromol. Theory. Simul. 9 (1), 1–13.
Wang, W., Barber, A.H., 2012. Measurement of size-dependent glass transition temperature in electrospun polymer fibers using AFM nanomechanical testing. J. Polym. Sci. B Polym. Phys. 50 (8), 546–551.
Wang, X., Ding, B., Li, B., 2013. Biomimetic electrospun nanofibrous structures for tissue engineering. Mater. Today 16 (6), 229–241.
Wang, L., et al., 2017. Electrospun conductive nanofibrous scaffolds for engineering cardiac tissue and 3D bioactuators. Acta Biomater. 59, 68–81.
Weishaupt, K., et al., 1995. Pressure dependence of the elastic constants of poly (methyl methacrylate). Polymer 36 (17), 3267–3271.

Wijnen, B., Sanders, P., Pearce, J.M., 2018. Improved model and experimental validation of deformation in fused filament fabrication of polylactic acid. Progress in Additive Manufacturing 3 (4), 193–203.
Wong, S.-C., Baji, A., Leng, S., 2008. Effect of fiber diameter on tensile properties of electrospun poly (ϵ-caprolactone). Polymer 49 (21), 4713–4722.
Wong, K.K.H., et al., 2009. Physical properties of ion beam treated electrospun poly (vinyl alcohol) nanofibers. Eur. Polym. J. 45 (5), 1349–1358.
Xue, J., et al., 2017. Electrospun nanofibers: new concepts, materials, and applications. Accounts Chem. Res. 50 (8), 1976–1987.
Yu, T.-Q., et al., 2010. Measure-preserving integrators for molecular dynamics in the isothermal–isobaric ensemble derived from the Liouville operator. Chem. Phys. 370 (1–3), 294–305.
Yun, K.M., et al., 2007. Nanoparticle filtration by electrospun polymer fibers. Chem. Eng. Sci. 62 (17), 4751–4759.
Zohuri, G., 2012. Polymer Science: a Comprehensive Reference.